A pause in Southern Hemisphere circulation trends due to the Montreal Protocol

https://doi.org/10.1038/s41586-020-2120-4

Received: 4 October 2019

Accepted: 29 January 2020

Published online: 25 March 2020

Check for updates

Antara Banerjee[1,2]✉, John C. Fyfe[3], Lorenzo M. Polvani[4], Darryn Waugh[5,6] & Kai-Lan Chang[1,2]

Observations show robust near-surface trends in Southern Hemisphere tropospheric circulation towards the end of the twentieth century, including a poleward shift in the mid-latitude jet[1,2], a positive trend in the Southern Annular Mode[1,3–6] and an expansion of the Hadley cell[7,8]. It has been established that these trends were driven by ozone depletion in the Antarctic stratosphere due to emissions of ozone-depleting substances[9–11]. Here we show that these widely reported circulation trends paused, or slightly reversed, around the year 2000. Using a pattern-based detection and attribution analysis of atmospheric zonal wind, we show that the pause in circulation trends is forced by human activities, and has not occurred owing only to internal or natural variability of the climate system. Furthermore, we demonstrate that stratospheric ozone recovery, resulting from the Montreal Protocol, is the key driver of the pause. Because pre-2000 circulation trends have affected precipitation[12–14], and potentially ocean circulation and salinity[15–17], we anticipate that a pause in these trends will have wider impacts on the Earth system. Signatures of the effects of the Montreal Protocol and the associated stratospheric ozone recovery might therefore manifest, or have already manifested, in other aspects of the Earth system.

Anthropogenic emissions of ozone depleting substances (ODSs) have been primarily responsible for stratospheric ozone depletion since around the 1960s, most strikingly in the springtime Antarctic ozone hole[18,19]. As a consequence, the Montreal Protocol of 1987, and its subsequent amendments and adjustments, were adopted to phase out global production and consumption of ODSs. The success of the Montreal Protocol has emerged since the late 1990s as declining inorganic halogen loadings in the stratosphere, commonly quantified by equivalent effective stratospheric chlorine (EESC)[20] and as ozone recovery in the upper stratosphere, most clearly in the northern mid-latitudes[21]. More recently, the Antarctic ozone hole has also begun to show signs of recovery[22,23].

Figure 1a illustrates Antarctic ozone depletion and its recovery in representative observations from the Solar Backscatter Ultraviolet (SBUV) system of total column ozone (TCO; black line) averaged over springtime (September–October–November, SON) and over the polar cap (poleward of 60° S) (Methods). The springtime ozone timeseries closely mirrors the rise and fall of polar EESC in winter[20,24] (red line; note the inverted *y* axis) when halogen reservoirs are converted into active (ozone-destroying) species in polar stratospheric clouds. Two piecewise continuous linear trend lines show the change from the ozone 'depletion period' to the 'recovery period', defined here as 1980–2000 and 2000–2017, respectively (Methods).

The ODS-induced ozone hole has, in turn, been the dominant cause of summertime trends in Southern Hemisphere (SH) atmospheric circulation. These include a poleward shift of the mid-latitude jet stream[9–11,25]; a positive trend in the Southern Annular Mode (SAM)[3,5,6,11,25], which is the dominant pattern of variability in the SH; an expansion of the overturning tropical circulation known as the Hadley cell[9–11,26]; and, related to that, an expansion of the subtropical dry zone[10,12]. In the presence of declining ODSs and EESC, and recovering Antarctic ozone (Fig. 1a), models robustly project future trends in SH tropospheric circulation to either cease or reverse[27–30]. In contrast, although rising CO_2 concentrations have contributed to poleward circulation trends in the recent past[6,9,31,32], their fairly monotonic increase is not expected to drive changes in trends. In this study, we seek to determine whether the projected ozone-driven changes are present in up-to-date reanalysis and observational records. Thus, beyond 'chemical' signatures of the Montreal Protocol—in EESC and stratospheric ozone—we show the emergence of its 'dynamical' signatures in atmospheric circulation.

Trends in near-surface circulation

We begin by considering three metrics of SH near-surface circulation: (1) the central latitude of the mid-latitude (or 'eddy-driven') jet at 850 hPa; (2) the SAM index; and (3) the latitude of the edge of the Hadley cell (Methods). Reanalysis values for these metrics are derived from four 'modern' products that extend to the present day: ERA-Interim (ERA-I)[33], the Japanese 55-yr reanalysis (JRA-55)[34] and the Modern-Era Retrospective Analysis for Research and Applications version 2 (MERRA2) analysis (-ana) and assimilation (-asm)[35]. For comparison with the reanalyses, the SAM index is also calculated from station-based observations of sea-level pressure[4].

For each metric and dataset, we calculate average SH summertime (December–January–February, DJF) values for each year over the

[1]Cooperative Institute for Research in Environmental Sciences, University of Colorado Boulder, Boulder, CO, USA. [2]Chemical Sciences Division, National Oceanic and Atmospheric Administration/Earth System Research Laboratory, Boulder, CO, USA. [3]Canadian Centre for Climate Modelling and Analysis, Environment and Climate Change Canada, Victoria, British Columbia, Canada. [4]Department of Applied Physics and Applied Mathematics, Columbia University, New York, NY, USA. [5]Department of Earth and Planetary Sciences, Johns Hopkins University, Baltimore, MD, USA. [6]School of Mathematics and Statistics, University of New South Wales, Sydney, New South Wales, Australia. ✉e-mail: antara.banerjee@noaa.gov

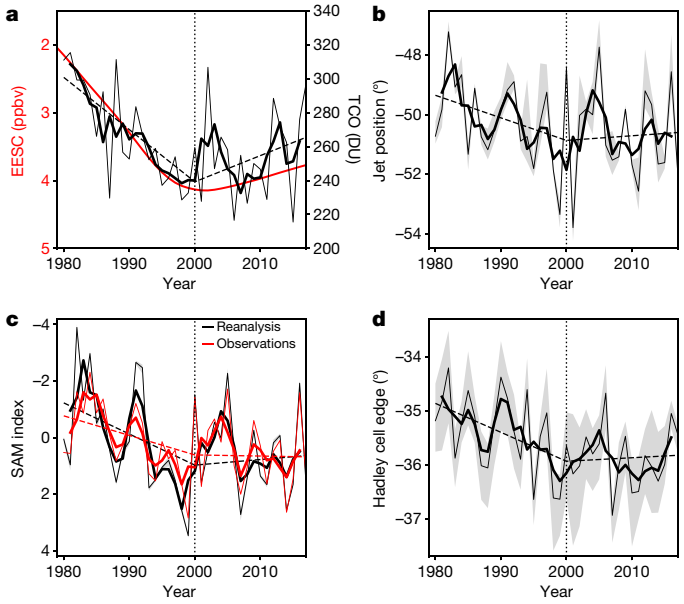

Fig. 1 | Timeseries of ozone and near-surface circulation metrics. a, EESC (note the inverted left *y* axis) for polar winter conditions and Antarctic TCO for the SON season as measured by SBUV (in Dobson units, DU). **b**–**d**, Circulation metrics for the DJF season. **b**, Position of the SH mid-latitude jet (in degrees latitude) in reanalysis data. **c**, SAM index (note the inverted *y* axis) as derived from reanalysis data and from station observations[4]. **d**, Latitude of the edge of the SH Hadley cell in reanalysis data. Thin black lines and the grey shaded envelopes in **b**–**d** represent the average across four reanalysis products (ERA-I, JRA-55, MERRA2-ana and MERRA2-asm) and their minimum to maximum range. Thin lines represent unsmoothed quantities and thick lines represent centred 3-yr smoothed values. Two piecewise continuous linear trend lines for the unsmoothed data (dashed lines) are drawn for the periods 1980–2000 and 2000–2017 (the values for their slopes are provided in Extended Data Table 1). ppbv, parts per billion by volume.

common observational period (1980–2017) and average across the reanalysis datasets (Methods). Figure 1b illustrates a robust poleward trend of the jet position in the depletion period that has been identified in previous observational studies[1,2]. However, the curve flattens around the year 2000 suggesting that a pause in poleward trends has occurred. By testing different change-points, we find that 2000 is the last year when poleward trends in the depletion period remain statistically significant at the 95% confidence level, whereas trends up to the year 2017 in the recovery period are not statistically significant for all change-points tested (Extended Data Table 1). The pause in poleward trends of the jet position is concurrent with Antarctic ozone recovery from around the year 2000.

Figure 1c demonstrates considerable agreement in the SAM timeseries among the different datasets, including the station-based observations (notice the small area shaded in grey). An increase in the SAM index during the depletion period is well established[1,3–6] and is further illustrated here (note the inverted *y* axis in Fig. 1c). We also identify a pause in the strengthening of the SAM, with the year 1999 being the last year in which positive reanalysis trends during the depletion period remain statistically significant; no significant trends are found in the recovery period (Extended Data Table 1). Depletion period trends in the observations are smaller than in the reanalysis average, but are significant at the 90% confidence level up to the year 2001 (Extended Data Table 1). Several studies have shown that the SAM confounds the jet properties of position, strength and width[2,36–38]. However, the mirrored long-term behaviour of the jet position and SAM index found here (compare Fig. 1b and c) supports a previous conclusion[38] that changes in the DJF SAM mostly reflect changes in the position of the jet. In contrast, the DJF jet strengthens at almost the same rate in the depletion and recovery periods (Extended Data Fig. 1 and Extended Data Table 1). Finally, the timeseries of the SH Hadley cell edge suggests that the poleward trend during the depletion period identified in previous studies[7,8] may also have paused during the recovery period (Fig. 1d), although the pause here is less clear, with depletion period trends remaining significant for all change-points tested (Extended Data Table 1).

These simple trend analyses indicate a pause in the SH near-surface circulation, and two features are consistent with changing ODSs as their driver. First, the pause around the year 2000 mirrors EESC and Antarctic TCO but stands in contrast to monotonically increasing CO_2 concentrations. Second, the pause occurs in DJF, consistent with a lagged seasonal signature of the ozone hole, but not in the opposing season (June–July–August, JJA; Extended Data Fig. 2). We now consider SH circulation trends through the troposphere and into the lower stratosphere, with the knowledge that near-surface climate changes due to the ozone hole occur as a result of coupling between the troposphere and stratosphere[3,9–11].

Trends in atmospheric zonal wind

Reanalysis trends

Here we examine piecewise linear trends in zonal wind in the observationally based reanalysis data, which we will refer to simply as observed trends hereafter. Zonal average zonal wind fields in DJF are averaged over the four reanalysis datasets before computing trends. The causal linkages between Antarctic stratospheric ozone and SH circulation identified in previous studies—only in modelled results for the recovery period[10,11,27–29]—are consistent with the observed trends found here. In the depletion period, ozone losses in the springtime Antarctic lower stratosphere result in local cooling trends at around 100 hPa through reduced absorption of solar radiation (Extended Data Fig. 3a). Via thermal wind balance, the local cooling is associated with a strengthening of the polar vortex and a delay in its break-up[39]. Strengthened zonal winds propagate downwards over the course of a few months (Extended Data Fig. 4a), extending to the surface in DJF (Fig. 2a). In contrast to the depletion period, the recovery period shows a statistically insignificant warming trend in the Antarctic lower stratosphere (Extended Data Fig. 3b), in broad agreement with previous reanalysis results[40]. Consistent with this trend, we do not identify any summertime wind response at the surface (Fig. 2b), and we find a reversal of the depletion period trends in January (Extended Data Fig. 4b). The pause is further illustrated by the change in trends between the two periods (Fig. 2c, Extended Data Fig. 4c).

Simulated trends

We now determine whether the observed zonal wind trends are reproduced in model simulations, using two distinct model ensembles. The first is a single-model, large initial-condition ensemble of simulations from the Canadian Earth System Model version 2 (CanESM2). Each member of the large ensemble utilizes identical forcings but slightly different initial conditions, leading to a spread of climate states across members. The model has a top near 1 hPa and prescribes ozone (Methods). The second is a multimodel ensemble of chemistry–climate models (CCMs). This comprises models that contributed to two well-documented intercomparison projects: the Chemistry-Climate Model Validation Activity phase 2 (CCMVal-2)[41] and its successor, the Chemistry-Climate Model Intercomparison (CCMI)[42] (Methods; Extended Data Table 2). Most of the CCMs are comprehensive models that are high-top (lid above 1 hPa) and calculate ozone concentrations online with interactive chemistry.

We first examine experiments using all known anthropogenic and natural (volcanic and solar) forcings (ALL-forcings). Fifty ALL-forcing simulations are available for each ensemble (Methods; Extended Data Table 2). Trends in zonal average zonal wind are computed for

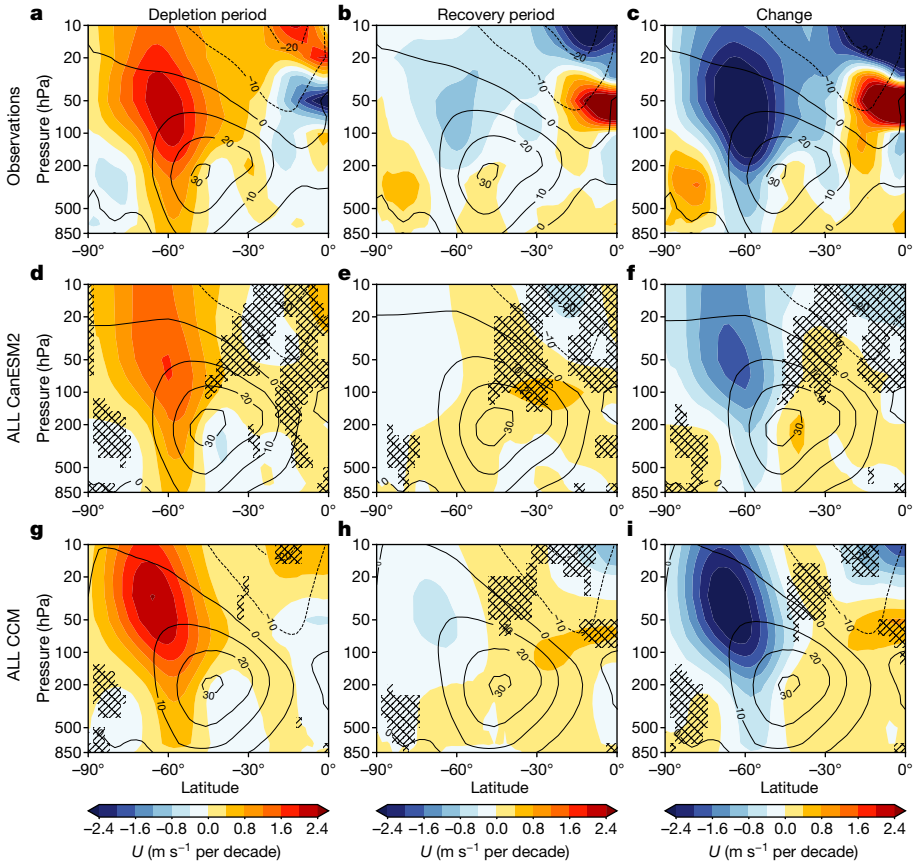

Fig. 2 | Zonal average zonal wind trends in reanalysis data and models. a–i, Latitude–altitude cross-sections of zonal average zonal wind trends (colour shading) for DJF are shown for the depletion period (**a**, **d**, **g**), recovery period (**b**, **e**, **h**) and the change between them (**c**, **f**, **i**). Trends for the four-reanalysis average (**a**–**c**) and the ALL fingerprints of CanESM2 (**d**–**f**) and the CCMs (**g**–**i**) are shown. Contours show climatological values (in m s^{-1}; in **c**, **f** and **i**, where the change is shown, the climatology is over the entire change period). The hatching in **d**–**i** shows areas where the reanalysis trends lie outside the 5th–95th percentile range of the simulated ALL ensemble trends.

each ensemble member and the 'fingerprints' of forced response are shown in Fig. 2d–i as ensemble means. These fingerprints bear a strong qualitative resemblance to the observed trends (Fig. 2a–c). Weaker trends are found in CanESM2 for the depletion period, which might in part reflect underestimated ozone loss prescribed in this model[43] and the resulting stratospheric cooling[44]. However, we also see from the unhatched areas in Fig. 2d–i that the observed trends in the mid-latitudes mostly fall within the 5–95% range of the modelled trends. Thus, the observed pause in zonal wind trends is reproduced by the models used here. The observed downward propagation of the mid-latitude zonal wind trends from the stratosphere to the troposphere is also broadly reproduced (Extended Data Fig. 4d–i). For the near-surface circulation metrics, the distribution of simulated ensemble trends confirms the connection with the stratospheric–tropospheric zonal wind response (Extended Data Fig. 5). Largely poleward trends in the jet position and positive trends in the SAM index during the depletion period transition to distributions that are more symmetric about zero in the recovery period (Extended Data Fig. 5a, b, d). A pause in poleward trends of the Hadley cell edge is also evident in the CCM ensemble (Extended Data Fig. 5e), although not in CanESM2 (Extended Data Fig. 5c).

We next examine experiments using individual forcings. The key advantage of the model ensembles used here over others—notably, the Coupled Model Intercomparison Project Phase 5 (CMIP5)—is the number and availability of simulations that allow the separation of the influences of greenhouse gases (GHGs) and stratospheric ozone (Methods; Extended Data Table 2).

We determine the role of stratospheric ozone (OZ) using a CanESM2 experiment forced by stratospheric ozone only (50 members); and the difference between the ALL and fixed-ODS (fODS; 21 members) experiments for the CCMs (technically giving the effect of ODSs, which here occur mainly through ozone; Methods). Comparing Fig. 2 and Fig. 3 (left columns) shows that under both ALL and OZ forcings, there are strengthening trends in stratospheric winds that extend to the surface during the depletion period (slightly weaker trends are found for OZ). In contrast to ALL, however, OZ shows a clear equatorward trend in the jet location during the recovery period (compare Fig. 2 and Fig. 3, middle columns). The trend change is similar between the two sets of experiments (compare Fig. 2 and Fig. 3, right columns).

We determine the role of GHGs as a residual in CanESM2, using 50-member ALL and single-forcing experiments; and the difference between the ALL and fixed-GHG (fGHG; 22 members) experiments for the CCMs (Methods). The model ensembles simulate weak trends in stratospheric winds and the jet location in both periods in response to GHGs. Overall, the results suggest that GHGs may have reinforced the effects of stratospheric ozone during the depletion period (Fig. 3g) and cancelled their effects during the recovery period (Fig. 3h, k). The change between the depletion and recovery periods in response to GHGs (Fig. 3i, l) does not match the pause in trends that is found in the reanalyses (Fig. 2c).

The spatial patterns of modelled trends in zonal wind support a contribution of stratospheric ozone forcing to the observed pause. Nevertheless, we need to discount the possibility that the observed pause occurred by chance (that is, due to internal variability of the climate system or natural forcings), noting that Antarctic stratospheric ozone itself can show large interannual variability (Fig. 1a). To this end, we now undertake a pattern-based detection and attribution analysis.

Detection and attribution

As the spatial pattern of the difference in the zonal average zonal wind trends between the depletion and recovery periods is a distinctive feature of the observed pause, a pattern-based detection and attribution approach is suitable (Methods). Simply put, we linearly regress the observed pattern of the trend change against the corresponding ALL fingerprints (Fig. 2c against Fig. 2f and i). The regression coefficients, or scaling factors, are shown in Fig. 4 and represent the factor by which the simulated fingerprints must be scaled to match the observations.

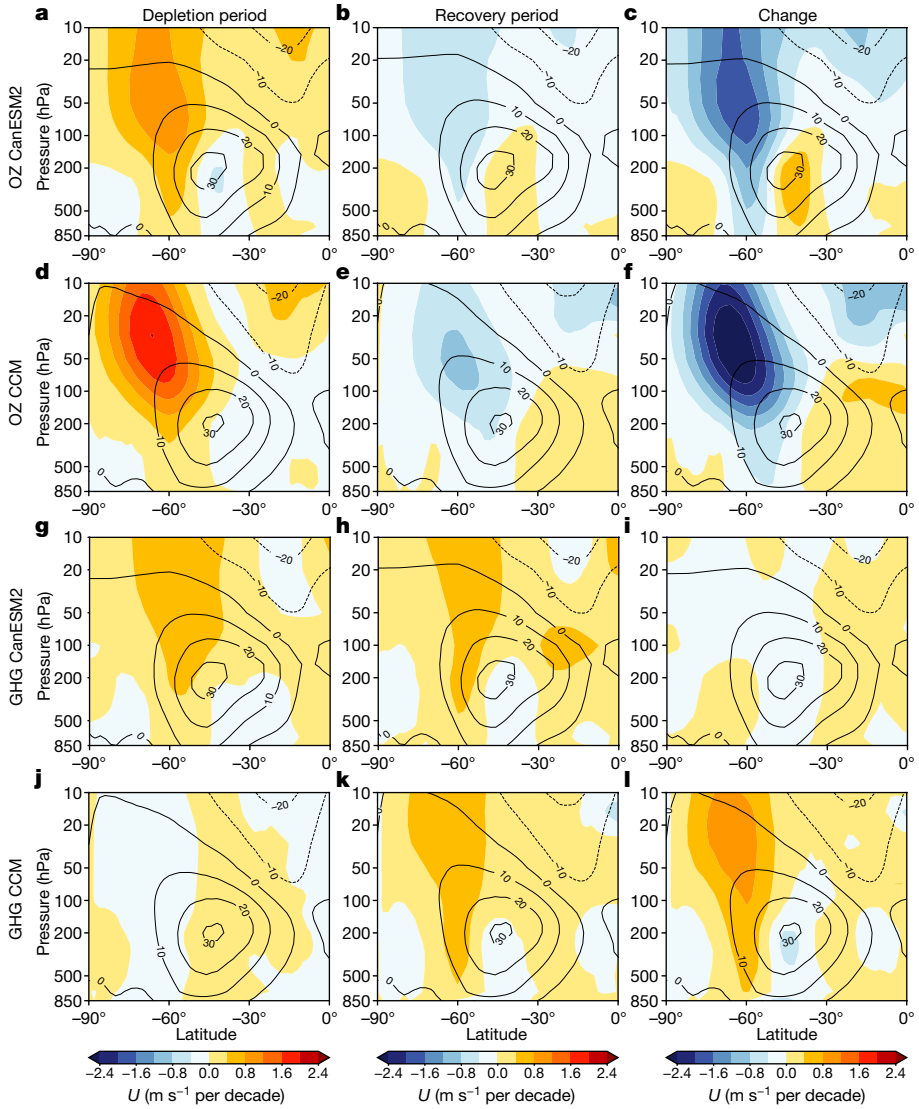

Fig. 3 | Simulated zonal average zonal wind trends due to stratospheric ozone and GHGs. Latitude–altitude cross-sections of zonal average zonal wind trends (colour shading) for DJF are shown for the depletion period, recovery period and the change between them. **a**–**l**, Fingerprints for the single forcings: OZ as simulated by CanESM2 (**a**–**c**) and by the CCMs (**d**–**f**); and GHGs as simulated by CanESM2 (**g**–**i**) and by the CCMs (**j**–**l**). For illustrative purposes, the contours represent the ALL forcing climatologies (in m s^{-1}; in **c**, **f** and **i**, the climatology is over the entire change period).

Uncertainties (vertical bars) represent the 2.5–97.5% (95%) range due to internal variability estimated from the ensemble spread across the CanESM2 members, or from a long pre-industrial control (piControl) simulation from one of the CCMs (WACCM4; see Methods). For both model ensembles, the scaling factors for the ALL fingerprints encompass unity and are distinct from zero at the 95% confidence level (Fig. 4). Thus, the observed pause is detected and we can rule out internal variability as its cause.

We next perform a multiple linear regression between the observed pattern of trend change against the corresponding OZ and GHG fingerprints (Methods). As with the ALL fingerprints, the scaling factors for both the CanESM2 and CCM ensembles' OZ fingerprints are consistent with unity (Fig. 4) and the observed pause is therefore formally attributed to stratospheric ozone. In contrast, the GHG scaling factors for the same model ensembles are consistent with zero (Fig. 4). Therefore, although our models suggest that increasing GHG concentrations have caused trends in the depletion and recovery periods (Fig. 3), they cannot be the cause of the observed pause in trends.

We perform additional sensitivity tests to determine the robustness of the detection and attribution conclusions to various parameter choices. First, we test the influence of forcings besides OZ and GHGs as simulated by CanESM2, specifically anthropogenic aerosols (AA) and natural forcings (NAT), which show weak zonal wind trends (Extended Data Fig. 6). When regressing the observed response against all four single-forcing fingerprints, we find that the scaling factors for AA and NAT have large confidence intervals that overlap zero (Extended Data Fig. 7, black lines), whereas the scaling factors for OZ and GHG remain similar to Fig. 4a. We can thus exclude anthropogenic aerosols and natural forcings as significant drivers of the observed pause. We further exclude the influence of solar natural variability by noting that the CCM-derived OZ and GHG confidence intervals remain robust to estimation from a 1,000-yr piControl run of one of the CCMs (WACCM4) that includes solar variability[40] (Methods; Extended Data Fig. 8, red lines). Our conclusions also remain robust, within at least 90% confidence, to various other parameters: using a smaller spatial domain of analysis, a subset of CCMs or estimating internal variability from a long piControl simulation of CanESM2 (Extended Data Figs. 7, 8).

In summary, the observed pause in zonal average zonal wind trends is detected and attributed to stratospheric ozone. Our conclusions regarding detectability are dependent on the realism of the models' simulation of internal variability. However, the similarity of results from two very different ensembles of models, and different forcing experiments, adds robustness to these conclusions.

Discussion and outlook

We have provided evidence from reanalyses and observations of the Southern Hemisphere that the poleward shift in summertime tropospheric circulation towards the end of the twentieth century, which has been widely documented, paused from around the year 2000.

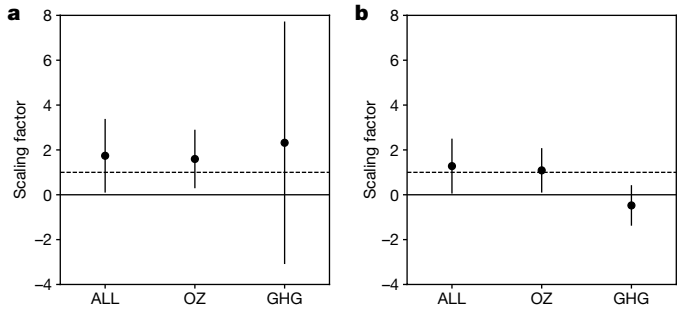

Fig. 4 | Scaling factors from the detection and attribution analysis. **a**, **b**, Scaling factors for CanESM2 (**a**) and CCMs (**b**) for the change in zonal average zonal wind trends between the depletion and recovery periods over the domain shown in Figs. 2, 3. The vertical bars represent the 95% uncertainty (2.5th–97.5th percentiles) from model-derived estimates of internal variability (Methods).

The observed response is here robustly reproduced by a diversity of models, which indicates that the recovery of stratospheric ozone—as a result of the Montreal Protocol—is the driver of the observed pause.

The consequences of the Montreal Protocol for tropospheric circulation should become even more apparent in the future. The pause (which is widely expected from model results) is only just beginning to emerge in the observations. The question then arises: as ODS concentrations presumably continue to decline but CO_2 concentrations presumably continue to rise, will the pause continue, or will there be a transition towards an equatorward-shifted extratropical jet, or will the poleward shifting resume? The answer will depend on the particular CO_2 (and other anthropogenic) emissions trajectory[45]. The combination of observations and integrated Earth system models will be crucial to detecting and attributing these changes within our complex climate system. The pre-2000 Southern Hemisphere circulation trends have had impacts on the weather and climate—on precipitation[12–14], and perhaps the ocean circulation and salinity[15–17], for example. We thus propose that the pause in these trends might have wider consequences for the Earth system that deserve further study.

Online content

Any methods, additional references, Nature Research reporting summaries, source data, extended data, supplementary information, acknowledgements, peer review information; details of author contributions and competing interests; and statements of data and code availability are available at https://doi.org/10.1038/s41586-020-2120-4.

1. Swart, N. C. & Fyfe, J. C. Observed and simulated changes in the Southern Hemisphere surface westerly wind-stress. *Geophys. Res. Lett.* **39**, L16711 (2012).
2. Swart, N. C., Fyfe, J. C., Gillett, N. & Marshall, G. J. Comparing trends in the Southern Annular Mode and surface westerly jet. *J. Clim.* **28**, 8840–8859 (2015).
3. Thompson, D. W. J. & Solomon, S. Interpretation of recent Southern Hemisphere climate change. *Science* **296**, 895–899 (2002).
4. Marshall, G. J. Trends in the Southern Annular Mode from observations and reanalyses. *J. Clim.* **16**, 4134–4143 (2003).
5. Gillett, N. P. & Fyfe, J. C. Annular mode changes in the CMIP5 simulations. *Geophys. Res. Lett.* **40**, 1189–1193 (2013).
6. Gillett, N. P., Fyfe, J. C. & Parker, D. E. Attribution of observed sea level pressure trends to greenhouse gas, aerosol, and ozone changes. *Geophys. Res. Lett.* **40**, 2302–2306 (2013).
7. Davis, S. M. & Rosenlof, K. H. A multidiagnostic intercomparison of tropical-width time series using reanalyses and satellite observations. *J. Clim.* **25**, 1061–1078 (2012).
8. Garfinkel, C. I., Waugh, D. W. & Polvani, L. M. Recent Hadley cell expansion: the role of internal atmospheric variability in reconciling modeled and observed trends. *Geophys. Res. Lett.* **42**, 10824–10831 (2015).
9. Son, S.-W. et al. Impact of stratospheric ozone on Southern Hemisphere circulation change: a multimodel assessment. *J. Geophys. Res. D* **115**, D00M07 (2010).
10. Polvani, L. M., Waugh, D. W., Correa, G. J. P. & Son, S.-W. Stratospheric ozone depletion: the main driver of twentieth-century atmospheric circulation changes in the Southern Hemisphere. *J. Clim.* **24**, 795–812 (2011).
11. McLandress, C. et al. Separating the dynamical effects of climate change and ozone depletion. Part II: Southern Hemisphere troposphere. *J. Clim.* **24**, 1850–1868 (2011).
12. Kang, S. M., Polvani, L. M., Fyfe, J. C. & Sigmond, M. Impact of polar ozone depletion on subtropical precipitation. *Science* **332**, 951–954 (2011).
13. Scheff, J. & Frierson, D. M. W. Robust future precipitation declines in CMIP5 largely reflect the poleward expansion of model subtropical dry zones. *Geophys. Res. Lett.* **39**, L18704 (2012).
14. Schmidt, D. F. & Grise, K. M. The response of local precipitation and sea level pressure to Hadley cell expansion. *Geophys. Res. Lett.* **44**, 10,573–10,582 (2017).
15. Waugh, D. W., Primeau, F., Devries, T. & Holzer, M. Recent changes in the ventilation of the southern oceans. *Science* **339**, 568–570 (2013).
16. Solomon, A., Polvani, L. M., Smith, K. L. & Abernathey, R. P. The impact of ozone depleting substances on the circulation, temperature, and salinity of the Southern Ocean: an attribution study with CESM1(WACCM). *Geophys. Res. Lett.* **42**, 5547–5555 (2015).
17. Karpechko, A. Y. & Maycock, A. C. in *Scientific Assessment of Ozone Depletion: 2018* Report No. 58, Ch. 5 (World Meteorological Organization, 2018).
18. Farman, J. C., Gardiner, B. G. & Shanklin, J. D. Large losses of total ozone in Antarctica reveal seasonal ClO_x/NO_x interaction. *Nature* **315**, 207–210 (1985).
19. Solomon, S., Garcia, R. R., Rowland, F. S. & Wuebbles, D. J. On the depletion of Antarctic ozone. *Nature* **321**, 755–758 (1986).
20. Engel, A. & Rigby, M. in *Scientific Assessment of Ozone Depletion: 2018* Report No. 58, Ch. 1 (World Meteorological Organization, 2018).
21. Braesicke, P. & Neu, J. et al. in *Scientific Assessment of Ozone Depletion: 2018* Report No. 58, Ch. 3 (World Meteorological Organization, 2018).
22. Solomon, S. et al. Emergence of healing in the Antarctic ozone layer. *Science* **353**, 269–274 (2016).
23. Langematz, U. & Tully, M. in *Scientific Assessment of Ozone Depletion: 2018* Report No. 58, Ch. 4 (World Meteorological Organization, 2018).
24. Engel, A. et al. A refined method for calculating equivalent effective stratospheric chlorine. *Atmos. Chem. Phys.* **18**, 601–619 (2018).
25. Gillett, N. P. & Thompson, D. W. J. Simulation of recent Southern Hemisphere climate change. *Science* **302**, 273–275 (2003).
26. Waugh, D. W., Garfinkel, C. I. & Polvani, L. M. Drivers of the recent tropical expansion in the Southern Hemisphere: changing SSTs or ozone depletion? *J. Clim.* **28**, 6581–6586 (2015).
27. Perlwitz, J., Pawson, S., Fogt, R. L., Nielsen, J. E. & Neff, W. D. Impact of stratospheric ozone hole recovery on Antarctic climate. *Geophys. Res. Lett.* **35**, L08714 (2008).
28. Son, S.-W. et al. The impact of stratospheric ozone recovery on the Southern Hemisphere westerly jet. *Science* **320**, 1486–1489 (2008).
29. Polvani, L. M., Previdi, M. & Deser, C. Large cancellation, due to ozone recovery, of future Southern Hemisphere atmospheric circulation trends. *Geophys. Res. Lett.* **38**, L04707 (2011).
30. Thompson, D. W. J. et al. Signatures of the Antarctic ozone hole in Southern Hemisphere surface climate change. *Nat. Geosci.* **4**, 741–749 (2011).
31. Arblaster, J. M. & Meehl, G. A. Contributions of external forcings to Southern Annular Mode trends. *J. Clim.* **19**, 2896–2905 (2006).
32. Barnes, E. A. & Polvani, L. Response of the midlatitude jets, and of their variability, to increased greenhouse gases in the CMIP5 models. *J. Clim.* **26**, 7117–7135 (2013).
33. Dee, D. P. et al. The ERA-Interim reanalysis: configuration and performance of the data assimilation system. *Q. J. R. Meteorol. Soc.* **137**, 553–597 (2011).
34. Kobayashi, S. et al. The JRA-55 Reanalysis: general specifications and basic characteristics. *J. Meteorol. Soc. Jpn* **93**, 5–48 (2015).
35. Gelaro, R. et al. The Modern-Era Retrospective Analysis for Research and Applications, Version 2 (MERRA-2). *J. Clim.* **30**, 5419–5454 (2017).
36. Monahan, A. H. & Fyfe, J. C. On the nature of zonal jet EOFs. *J. Clim.* **19**, 6409–6424 (2006).
37. Monahan, A. H. & Fyfe, J. C. On annular modes and zonal jets. *J. Clim.* **21**, 1963–1978 (2008).
38. Solomon, A. & Polvani, L. M. Highly significant responses to anthropogenic forcings of the midlatitude jet in the Southern Hemisphere. *J. Clim.* **29**, 3463–3470 (2016).
39. Sun, L., Chen, G. & Robinson, W. A. The role of stratospheric polar vortex breakdown in Southern Hemisphere climate trends. *J. Atmos. Sci.* **71**, 2335–2353 (2014).
40. Solomon, S. et al. Mirrored changes in Antarctic ozone and stratospheric temperature in the late 20th versus early 21st centuries. *J. Geophys. Res. D* **122**, 8940–8950 (2017).
41. Morgenstern, O. et al. Review of the formulation of present-generation stratospheric chemistry-climate models and associated external forcings. *J. Geophys. Res.* **115**, D00M02 (2010).
42. Morgenstern, O. et al. Review of the global models used within phase 1 of the Chemistry–Climate Model Initiative (CCMI). *Geosci. Model Dev.* **10**, 639–671 (2017).
43. Cionni, I. et al. Ozone database in support of CMIP5 simulations: results and corresponding radiative forcing. *Atmos. Chem. Phys.* **11**, 11267–11292 (2011).
44. Santer, B. D. et al. Quantifying stochastic uncertainty in detection time of human-caused climate signals. *Proc. Natl Acad. Sci. USA* **116**, 19821–19827 (2019); correction **117**, 2723 (2020).
45. Barnes, E. A., Barnes, N. W. & Polvani, L. M. Delayed Southern Hemisphere climate change induced by stratospheric ozone recovery, as projected by the CMIP5 models. *J. Clim.* **27**, 852–867 (2014).

Methods

Observations and reanalyses

TCO observations are from version 8.6 of the SBUV satellite dataset, using the 5° gridded, monthly and zonal mean products. Values in Fig. 1a are averaged over the polar cap (60–90° S) and springtime (SON).

EESC shown in Fig. 1a is the inverted timeseries of the values shown in figure 1-18a (red line) of the *Scientific Assessment of Ozone Depletion: 2018* (SAP-2018)[20]. These values are representative of polar winter conditions, with a mean age of stratospheric air of 5.5 years. A recent formulation of EESC updates the fractional release factors used in its calculation[46] from those used in an older method[24]; we arbitrarily use the latter as the two methods differ negligibly in polar winter conditions (compare the red and black lines in Fig. 1-18a of SAP-2018[20]).

Our analysis of recent SH circulation changes is centred on four reanalysis products: ERA-I[33], JRA-55[34] and MERRA2-ana and MERRA2-asm[35]. These are the most recent reanalyses and are used in preference to older generation products, which can show spurious trends and greater disagreement than newer reanalyses and climate models in metrics of the mid-latitude jet and tropical width[2,47,48]. We use both available MERRA products, as their differences—in particular for tropical width trends[8]—are part of the observational uncertainty that we wish to sample. We also use only those reanalyses that extend to the present day. The common period for analysis is therefore January 1980 to February 2018.

For the SAM, we also compute the index from observed sea-level pressures from 12 stations[4], using monthly mean, proxy zonal mean pressures at 40° S and 65° S.

Models

We use simulations from the CanESM2 model[49], a coupled atmosphere–ocean model that contributed to CMIP5. The atmospheric component is the Canadian Atmospheric Global Climate model (CanAM4) at T63 horizontal resolution (~1.88°) and 35 vertical levels with a top at 1 hPa.

Simulations with this model include large initial-condition ensembles performed under different external forcing scenarios (each member has the same forcing but slightly different initial conditions). We analyse the all-forcing (all known anthropogenic and natural) scenario (ALL) and the single-forcing scenarios: (1) OZ (stratospheric ozone), (2) AA (anthropogenic aerosols) and (3) NAT (natural) forcings. The scenarios follow CMIP5 forcing recommendations, including a time-varying ozone database for prescribing ozone, which slightly underestimates the depth of the ozone hole and the resulting cooling[43,44]. The historical period ends in 2005 and the simulations follow the RCP8.5 emissions scenario from 2006 onwards. While this is a relatively high-emissions scenario, there are only small differences in global CO_2 concentration and radiative forcing between the range of RCP scenarios for the period of analysis considered here[50]. Looking beyond our analysis period, the CO_2 forcing in the RCP8.5 scenario would provide a strong counteracting influence against the impacts of ozone recovery.

The ensemble of CCMs used here comprises models from two intercomparison projects: CCMVal-2[41] and CCMI[42]. Most participating models resolve the stratosphere (model tops above 1 hPa) and all contain comprehensive representations of stratospheric chemistry, including fully interactive ozone. The majority of models are not coupled to the ocean, which should not be crucial to determining the SH tropospheric circulation response to stratospheric ozone changes[51]. These model intercomparisons have provided insight into the observed SH climate response to polar ozone changes[9,52]. While the models can show considerable biases in their climatological jet position compared with observations[9,52], the biases do not seem to correlate with trends, and intermodel spread is instead substantially driven by interannual variability[53]. Given large intermodel differences in the response of the jet position to stratospheric ozone changes[53,54], we use every available ensemble member from each CCM with relevant output.

The experiments analysed are ALL, fGHG and fODS forcings. Sea surface temperatures and sea ice are prescribed in most models using output from coupled model simulations, while a minority of the models are coupled to an ocean. In fGHG, for consistency with the GHG radiative forcing, the climatological average sea surface temperature and sea ice over the period 1955–1964 are prescribed. Both intercomparisons follow the same ODS scenario (WMO A1). They differ in their GHG scenario, with CCMVal-2 following SRES A1B and CCMI following RCP6.0, but the differences in radiative forcing for the period of analysis in this study are minimal.

The CCM intercomparisons did not include any control runs. We instead obtain a piControl run from CESM1, with the atmosphere modelled by WACCM4. This is the same model that contributed to the CCMI project. The model is high top (~140 km) with 66 vertical levels and a horizontal resolution of 1.9° × 2.5° (latitude × longitude); the piControl is a 200-yr run, performed under fixed and unchanging pre-industrial (1850) external forcings[55]. We use a further control run, performed with the same model, under pre-industrial conditions but containing natural forcing as the 11-yr solar cycle[40].

In summary, our two ensembles contain a diverse range of models, each with their own strengths: CanESM2 captures atmosphere–ocean interactions, and this single-model large ensemble allows for a clean separation of forcing from internal variability; the CCMs simulate stratospheric chemistry, and this multimodel ensemble captures model uncertainty. Both ensembles contain experiments that allow us to isolate the impacts of single forcings, such as stratospheric ozone and GHGs, against a background of internal variability.

Metrics of SH circulation

Gridded monthly-mean fields of sea-level pressure, zonal wind and meridional wind are first averaged zonally and seasonally. This study focuses on the DJF season, for which the mean is taken over December of the labelled year and January–February of the subsequent year. The metrics of SH circulation are then calculated from seasonal mean fields as follows:

1. The SAM index is the difference between normalized zonal average sea-level pressures at 40° S and 65° S (ref. [56]), using the normalization period (1980–2000) common to the data used here. Sea-level pressure output was not available for the CCMs for computation of the SAM index.
2. The strength of the mid-latitude jet is the maximum near-surface (850 hPa) zonal average zonal wind, and the position is the latitude at which this maximum occurs. This is found in gridded data by analytically fitting a quadratic between the latitude of the largest value and the two latitudes either side.
3. The commonly used mass streamfunction approach is adopted to quantify the edge of the Hadley cell, which is found to provide a suitable measure of the width of the tropics[57–59]. The southern edge of the Hadley cell is the zero-crossing latitude of the mean meridional streamfunction at 500 hPa in the SH, calculated from the meridional wind. This is found in gridded data by linear interpolation between the latitudes on either side of the zero crossing.

Choice of time periods

Timeseries of ozone and circulation metrics in Fig. 1 include two piecewise continuous linear trends, computed using generalized least squares regression with noise modelled by an autoregressive process of order 1 (AR(l))[60]. Slope values and 95% confidence intervals for Fig. 1 (calculated as 1.96σ, where σ is the standard error of the slope) are shown in Extended Data Table 1. After testing numerous change-points (Extended Data Table 1), we find that 1997 (and more clearly, 1998) is when TCO trends in the recovery period first become statistically significant at the 95% confidence level, whereas EESC reaches a maximum in the year 2002 (Fig. 1). We therefore select a change-point at year 2000, which lies between these dates and is consistent with WMO

SAP-2018[23]. Given that increasing EESC and Antarctic ozone depletion have driven trends in SH circulation metrics, and the hypothesis that these trends will cease or reverse under ozone recovery, the same time periods are used for the circulation metrics.

We have chosen not to exclude any years in our analysis, acknowledging that internal variability (for example, warm years with high ozone caused by dynamical variability of the Antarctic polar vortex) might affect our calculated trends. The influence of internal variability in driving the SH circulation pause is instead ruled out, as far as possible, using the pattern-based detection and attribution analysis.

Simulated trends due to OZ and GHGs

CanESM2. The OZ trends are calculated using the 50-member OZ single-forcing experiment. The GHG simulation was not performed, but GHG-driven trends are derived as a residual by subtracting the sum of trends in OZ, AA and NAT from the ALL forcing trend; that is, GHG = ALL − (OZ + AA + NAT), assuming additivity in the response to single forcings.

CCMs. The OZ and GHG fingerprints are obtained by ALL − fODS and ALL − fGHG, respectively. The OZ fingerprint is technically a fingerprint of ODSs, but these species impact on surface SH circulation primarily through stratospheric ozone. ODSs are also GHGs, but their direct radiative impact on the surface SH circulation is also small compared to the effect of CO_2; GHG trends derived from the fGHG simulation should therefore mainly reflect the impact of CO_2.

Detection and attribution

We adopt a pattern-based fingerprinting approach that implements one-signal and multisignal analysis for detection and attribution[61]. The response that we analyse is the change in zonal average zonal wind trends between the depletion and recovery periods. Fingerprints refer to the ensemble mean of modelled responses and regressions are performed for the domain shown in Figs. 2, 3 (10–850 hPa and 0–90° S). All fields are first interpolated onto a common resolution of 2° × 2° (latitude × longitude) and 31 pressure levels (the standard CMIP5/CCMVal-2/CCMI vertical grid).

Scaling factors

The scaling factor is the factor by which the simulated fingerprint must be scaled up or down to match the observation.

In our one-signal analysis, we compute a fit using simple linear regression to obtain the ALL forcing scaling factors:

$$y = \beta^{\mathrm{ALL}} f^{\mathrm{ALL}} + \beta^0$$

where y is the observed trend, f^{ALL} is the modelled ALL forcing fingerprint of the trend (that is, in ALL CanESM2 or ALL CCM), the β^{ALL} regression coefficient is the scaling factor and β^0 is a constant.

In our two-signal analysis, we compute a fit using multiple linear regression:

$$y = \beta^{\mathrm{OZ}} f^{\mathrm{OZ}} + \beta^{\mathrm{GHG}} f^{\mathrm{GHG}} + \beta^0$$

where f^{OZ} and f^{GHG} are the modelled fingerprints of the trends due to OZ and GHG, and the β^{OZ} and β^{GHG} regression coefficients are the corresponding scaling factors.

Although there are forcings besides stratospheric ozone and GHGs, these probably suffice as explanatory variables for the SH circulation response. This is confirmed by a sensitivity test, which performs a multisignal analysis that also considers the simulated responses to anthropogenic aerosols and natural forcings in CanESM2 (see the main text and results in Extended Data Fig. 7):

$$y = \beta^{\mathrm{OZ}} f^{\mathrm{OZ}} + \beta^{\mathrm{GHG}} f^{\mathrm{GHG}} + \beta^{\mathrm{AA}} f^{\mathrm{AA}} + \beta^{\mathrm{NAT}} f^{\mathrm{NAT}} + \beta^0$$

where f^{OZ}, f^{GHG}, f^{AA} and f^{NAT} are the CanESM2 modelled fingerprints, and the β^{OZ}, β^{GHG}, β^{AA} and β^{NAT} regression coefficients are the corresponding scaling factors.

Uncertainties. The uncertainties around each scaling factor are model-derived estimates of internal variability. For CanESM2, internal variability is estimated from the intra-ensemble spread. The fingerprint ($\bar{x}_j$) of each experiment, j, is subtracted from the response ($x_{i,j}$) in each realization, i, to give residuals ($x'_{i,j}$) that represent different realizations of internal variability:

$$x'_{i,j} = x_{i,j} - \bar{x}_j \quad i = 1\ldots50\,;\, j = 1\ldots4$$

where the ranges reflect 50 members in four experiments. As with the observation, each $x'_{i,j}$ is individually regressed with one-signal or multisignal analysis against the CanESM2 modelled fingerprints:

$$x'_{i,j} = \beta^{\mathrm{ALL}}_{i,j} f^{\mathrm{ALL}} + \beta^0$$

$$x'_{i,j} = \beta^{\mathrm{OZ}}_{i,j} f^{\mathrm{OZ}} + \beta^{\mathrm{GHG}}_{i,j} f^{\mathrm{GHG}} + \beta^0$$

$$x'_{i,j} = \beta^{\mathrm{OZ}}_{i,j} f^{\mathrm{OZ}} + \beta^{\mathrm{GHG}}_{i,j} f^{\mathrm{GHG}} + \beta^{\mathrm{AA}}_{i,j} f^{\mathrm{AA}} + \beta^{\mathrm{NAT}}_{i,j} f^{\mathrm{NAT}} + \beta^0$$

$$i = 1\ldots50;\; j = 1\ldots4$$

The 2.5th–97.5th percentile range of the 200 regression coefficients gives the 95% confidence interval around each scaling factor. Extended Data Fig. 7 also shows the 5–95% (90%) range.

The uncertainty around the CCM scaling factors is derived from the WACCM4 200-yr piControl run. The response is calculated for consecutive 38-yr segments (that is, the difference between the 21-yr and 18-yr piecewise linear trends in each segment, consistent with the ozone depletion and recovery periods 1980–2000 and 2000–2017, to give 162 realizations of internal variability). These are regressed with one-signal analysis against the ALL CCM fingerprint, and two-signal analysis against the OZ CCM and GHG CCM fingerprints. The 2.5th–97.5th percentile range of the 162 regression coefficients gives the 95% confidence interval around each scaling factor. Extended Data Fig. 8 also shows the 5–95% (90%) range.

Further sensitivity tests (see main text and Extended Data Figs. 7, 8) show that the confidence intervals are relatively robust to other measures of internal/natural variability: as derived from a 296-yr CanESM2 piControl run and a 1,000-yr WACCM piControl run that also contains natural (solar) forcing[40].

Data availability

Observations of total column ozone from the SBUV v8.4 satellite dataset (5° gridded, monthly and zonal mean) are available at: https://acd-ext.gsfc.nasa.gov/Data_services/merged/data/sbuv_v86_mod.int_lyr.70-17.za.r6_ext.txt.The reanalysis datasets can be downloaded from their respective webservers, provided by the European Centre for Medium-Range Weather Forecasts (ECMWF) for ERA-I (https://apps.ecmwf.int/datasets/data/interim-full-daily/levtype=sfc/), the JMA Data Dissemination System (JDDS) for JRA-55 (https://jra.kishou.go.jp/JRA-55/index_en.html#download) and the Goddard Earth Sciences Data and Information Services Center (GES DIC) for MERRA2 (https://disc.gsfc.nasa.gov/datasets?keywords=%22MERRA-2%22&page=1&source=Models%2FAnalyses%20MERRA-2). Monthly

mean, proxy zonal mean pressures at 40° S and 65° S, used here to compute the observed SAM index, are available at: http://www.nerc-bas.ac.uk/icd/gjma/sam.html. Model output for CanESM2 can be accessed at: http://climate-modelling.canada.ca/climatemodeldata/cgcm4/CanESM2/index.shtml. Model output from CCMI and CCMVal-2 can be accessed through the British Atmospheric Data Center (BADC) archive at: ftp://ftp.ceda.ac.uk. The two WACCM control simulations are available from the High Performance Storage System at the National Center for Atmospheric Research in Boulder, Colorado and available upon request from the corresponding author.

Code availability

Code is available from the corresponding author upon reasonable request.

46. Newman, P. A., Daniel, J. S., Waugh, D. W. & Nash, E. R. A new formulation of equivalent effective stratospheric chlorine (EESC). *Atmos. Chem. Phys.* **7**, 4537-4552 (2007).
47. Davis, N. A. & Davis, S. M. Reconciling Hadley cell expansion trend estimates in reanalyses. *Geophys. Res. Lett.* **45**, 11439–11446 (2018).
48. Grise, K. M. et al. Recent tropical expansion: natural variability or forced response? *J. Clim.* **32**, 1551–1571 (2019).
49. Arora, V. K. et al. Carbon emission limits required to satisfy future representative concentration pathways of greenhouse gases. *Geophys. Res. Lett.* **38**, L05805 (2011).
50. van Vuuren, D. P. et al. The representative concentration pathways: an overview. *Clim. Change* **109**, 5 (2011).
51. Sigmond, M., Fyfe, J. C. & Scinocca, J. F. Does the ocean impact the atmospheric response to stratospheric ozone depletion? *Geophys. Res. Lett.* **37**, L12706 (2010).
52. Son, S.-W. et al. Tropospheric jet response to Antarctic ozone depletion: an update with Chemistry-Climate Model Initiative (CCMI) models. *Environ. Res. Lett.* **13**, 054024 (2018).
53. Seviour, W. J. M., Waugh, D. W., Polvani, L. M., Correa, G. J. P. & Garfinkel, C. I. Robustness of the simulated tropospheric response to ozone depletion. *J. Clim.* **30**, 2577–2585 (2017).
54. Gerber, E. P. & Son, S.-W. Quantifying the summertime response of the austral jet stream and Hadley cell to stratospheric ozone and greenhouse gases. *J. Clim.* **27**, 5538–5559 (2014).
55. Smith, K. L., Neely, R. R., Marsh, D. R. & Polvani, L. M. The Specified Chemistry Whole Atmosphere Community Climate Model (SC-WACCM). *J. Adv. Model. Earth Syst.* **6**, 883–901 (2014).
56. Gong, D. & Wang, S. Definition of Antarctic Oscillation index. *Geophys. Res. Lett.* **26**, 459–462 (1999).
57. Solomon, A., Polvani, L. M., Waugh, D. W. & Davis, S. M. Contrasting upper and lower atmospheric metrics of tropical expansion in the Southern Hemisphere. *Geophys. Res. Lett.* **43**, 10496–10503 (2016).
58. Davis, N. & Birner, T. On the discrepancies in tropical belt expansion between reanalyses and climate models and among tropical belt width metrics. *J. Clim.* **30**, 1211–1231 (2017).
59. Waugh, D. W. et al. Revisiting the relationship among metrics of tropical expansion. *J. Clim.* **31**, 7565–7581 (2018).
60. Weatherhead, E. C. et al. Factors affecting the detection of trends: statistical considerations and applications to environmental data. *J. Geophys. Res.* **103**, 17149–17161 (1998).
61. Swart, N. C., Gille, S. T., Fyfe, J. C. & Gillett, N. P. Recent Southern Ocean warming and freshening driven by greenhouse gas emissions and ozone depletion. *Nat. Geosci.* **11**, 836–841 (2018).

Acknowledgements We thank J. Daniel, N. A. Davis, S. M. Davis and B. Santer for conversations on this work. This work was funded by grants from the US National Science Foundation (NSF) to Columbia University and a fellowship from the Cooperative Institute for Research in Environmental Sciences (CIRES).

Author contributions A.B. proposed the paper, performed the analysis and wrote the paper. A.B. and J.C.F. designed the paper and interpreted the results, with contributions from L.M.P. and D.W. K-L.C. advised on statistical methods.

Competing interests The authors declare no competing interests.

Additional information

Correspondence and requests for materials should be addressed to A.B.

Peer review information *Nature* thanks Sandip Dhomse, Alexey Karpechko, Wenshou Tian and Guang Zeng for their contribution to the peer review of this work.

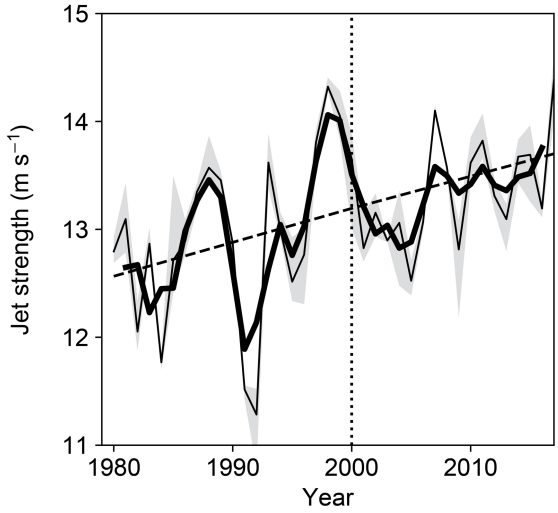

Extended Data Fig. 1 | Timeseries of mid-latitude jet strength. The timeseries is for the DJF season. Thin black lines and the grey shaded envelope represent the average across four reanalysis products (ERA-I, JRA-55, MERRA2-ana and MERRA2-asm) and their minimum to maximum range. The thin line represents the unsmoothed quantity and the thick line represents centred 3-yr smoothed values. Two piecewise continuous linear trend lines for the unsmoothed data (dashed lines) are drawn for the periods 1980–2000 and 2000–2017 (the values for their slopes are provided in Extended Data Table 1).

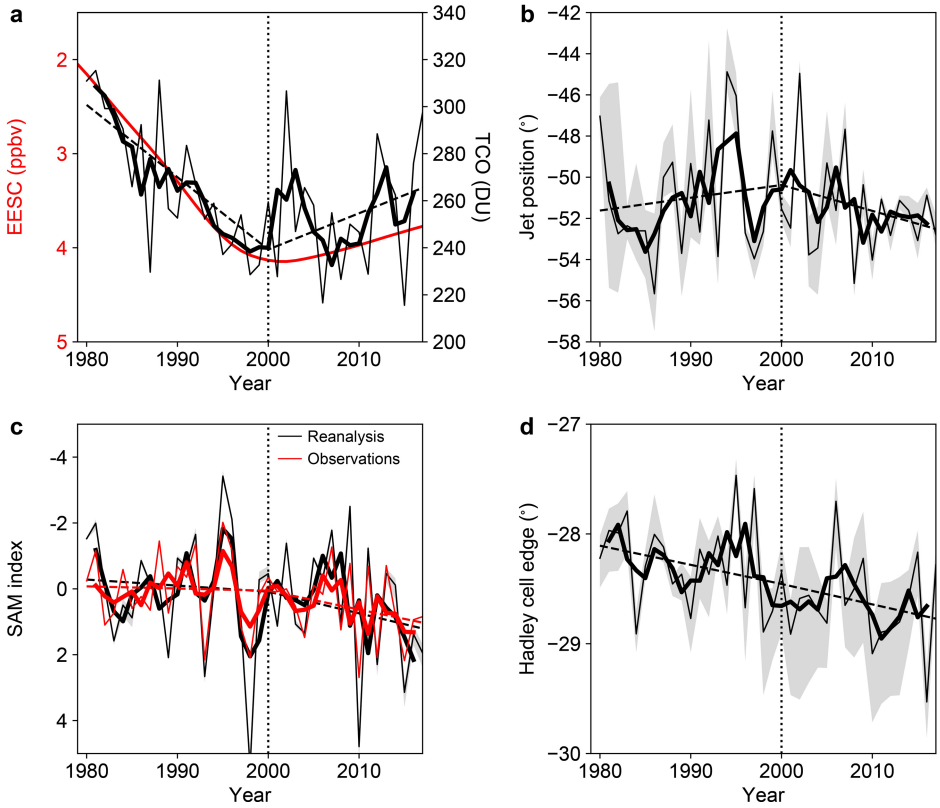

Extended Data Fig. 2 | Timeseries of ozone and near-surface circulation metrics. a, EESC (note the inverted left *y* axis) for polar winter conditions and Antarctic TCO for the SON season as measured by SBUV (in Dobson units, DU). **b**–**d**, Circulation metrics for the JJA season. **b**, Position of the SH mid-latitude jet (in degrees latitude) in reanalysis data. **c**, SAM index (note the inverted *y* axis) as derived from reanalysis data and from station observations[4]. **d**, Latitude of the edge of the SH Hadley cell in reanalysis data. Thin black lines and grey shaded envelopes in **b**–**d** represent the average across four reanalysis products (ERA-I, JRA-55, MERRA2-ana and MERRA2-asm) and their minimum to maximum range. Thin lines represent unsmoothed quantities and thick lines represent centred 3-yr smoothed values. Two piecewise continuous linear trend lines for the unsmoothed data (dashed lines) are drawn for the periods 1980–2000 and 2000–2017.

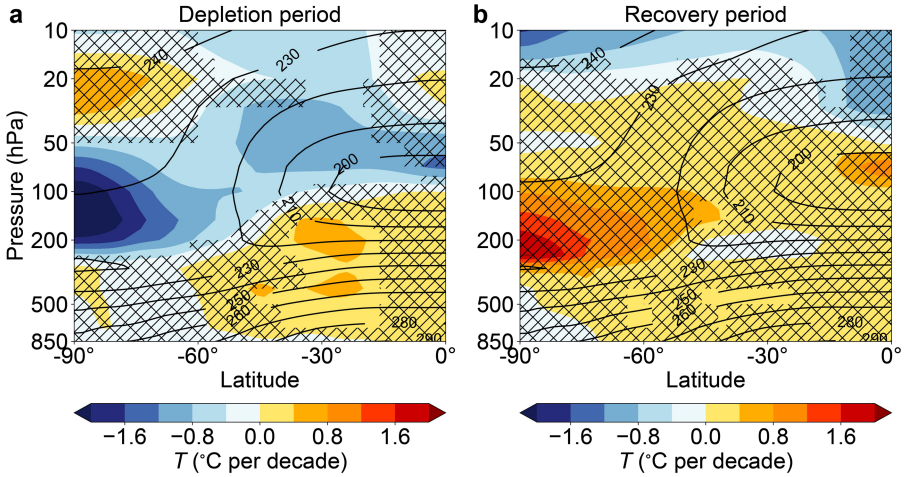

Extended Data Fig. 3 | Zonal average temperature trends. a, **b**, Latitude–altitude cross-sections of zonal average temperature trends (colour shading) for SON are shown for the depletion period (**a**) and recovery period (**b**). Trends are for the four-reanalysis average. Contours show climatological values (in °C). Hatching indicates areas where trends are not significant at the 95% confidence level according to a two-tailed Student's *t*-test using the standard error in the slopes.

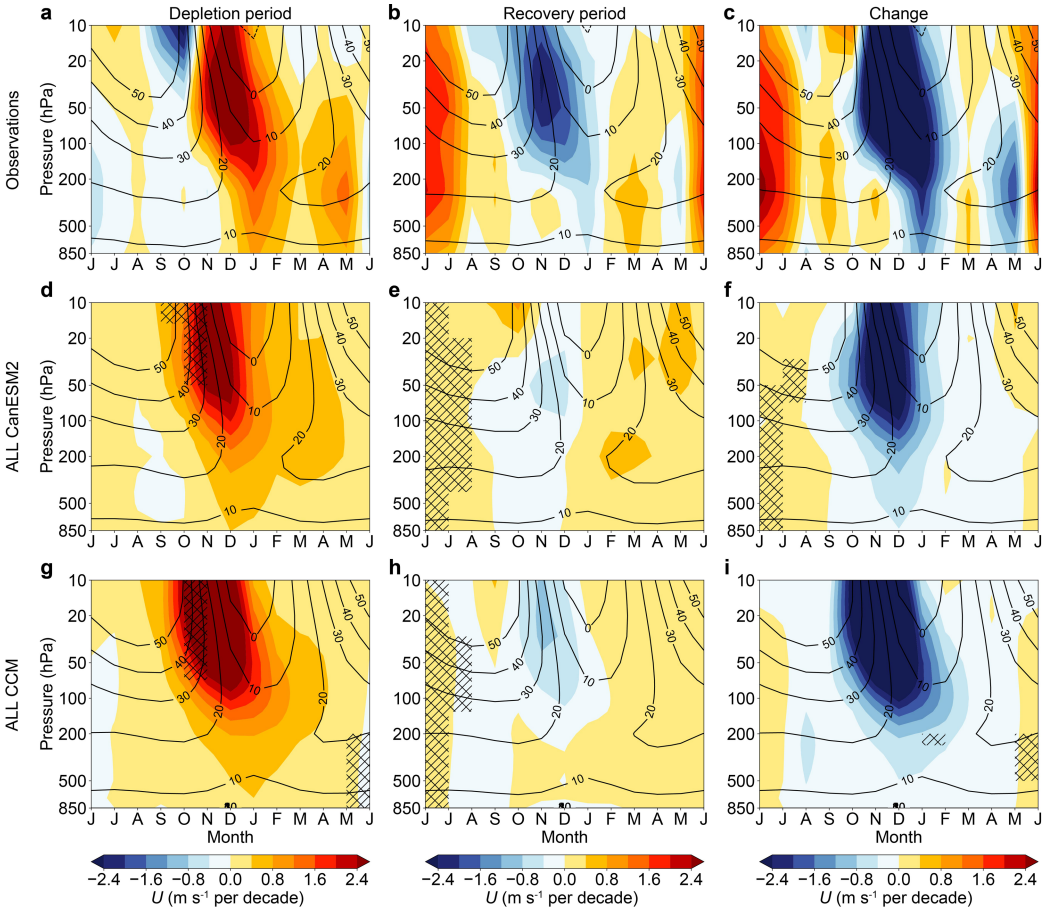

Extended Data Fig. 4 | Monthly trends in mid-latitude zonal wind. The monthly evolution of trends in latitudinally averaged (50–70° S) zonal wind (colour shading) for DJF are shown for the depletion period (**a**, **d**, **g**), recovery period (**b**, **e**, **h**) and the change between them (**c**, **f**, **i**). **a**–**i**, Trends for the four-reanalysis average (**a**–**c**) and the ALL fingerprints of CanESM2 (**d**–**f**) and the CCMs (**g**–**i**) are shown. Contours show climatological values (in m s^{-1}; in **c**, **f** and **i**, the climatology is over the entire change period). The hatching in **d**–**i** shows areas where the reanalysis trends lie outside the 5th–95th percentile range of the simulated ALL ensemble trends.

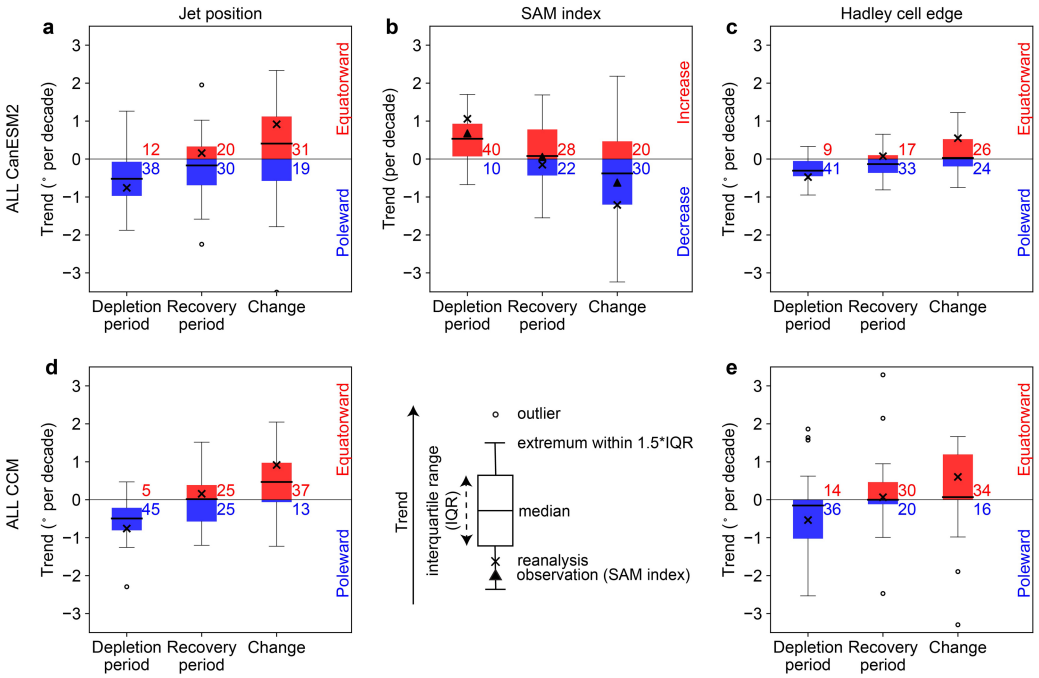

Extended Data Fig. 5 | Simulated trends in near-surface circulation metrics. **a**–**e**, Standard box and whisker plots showing DJF trends in jet position (**a**, **d**; degrees latitude per decade), the SAM index (**b**; per decade) and the Hadley cell edge (**c**, **e**; degrees latitude per decade) across the CanESM2 (**a**–**c**) and CCM (**d**, **e**) ensembles. Numbers designate the number of ensemble members showing positive (red) and negative (blue) trends. The cross symbols represent the average trends across the four reanalysis products. For the SAM index, the triangles represent trends in station-based observations.

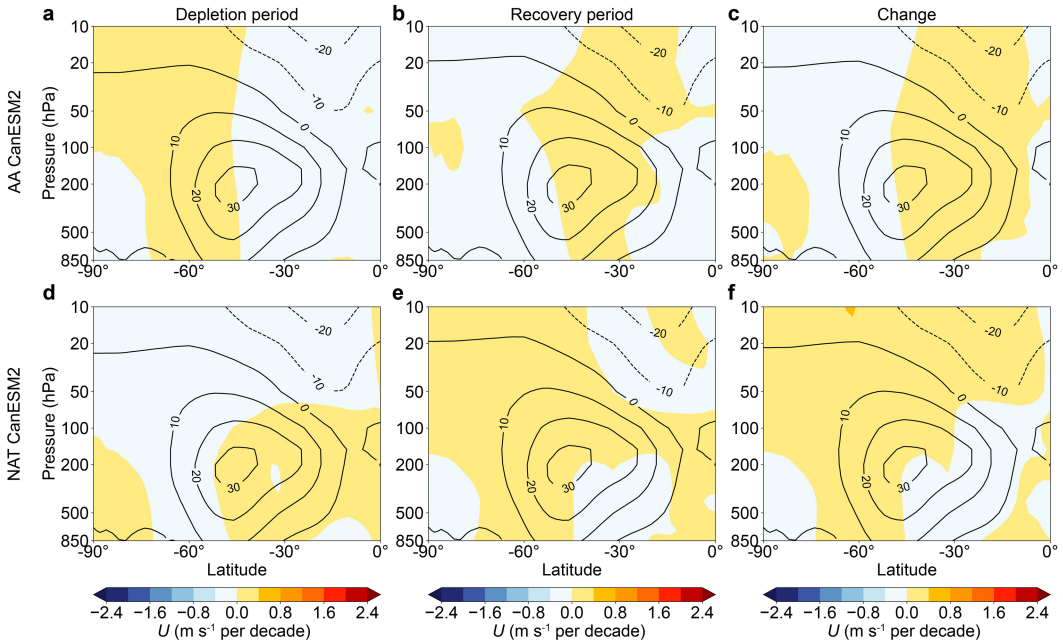

Extended Data Fig. 6 | Simulated zonal average zonal wind trends due to anthropogenic aerosols and natural forcing. Latitude–altitude cross-sections of zonal average zonal wind trends (colour shading) for DJF are shown for the depletion period (**a**, **d**), recovery period (**b**, **e**) and the change between them (**c**, **f**). **a**–**f**, Fingerprints for the single forcings: AA (**a**–**c**) and NAT (**d**–**f**) as simulated by CanESM2. For illustrative purposes, the contours represent the ALL forcing climatologies (in m s^{-1}; in **c** and **f**, the climatology is over the entire change period).

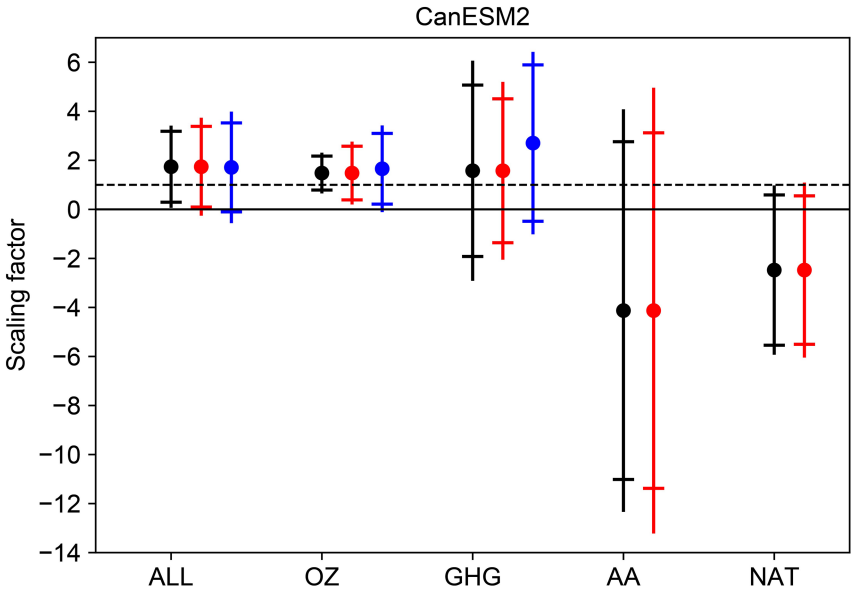

Extended Data Fig. 7 | Scaling factors from detection and attribution sensitivity tests for CanESM2. The main analysis (Fig. 4a) considers a one-signal analysis against the ALL fingerprint, and a two-signal analysis against the OZ and GHG fingerprints, where confidence intervals are derived from the ensemble spread, and over the domain shown in Figs. 2, 3 (10–850 hPa, 0–90° S). The sensitivity tests shown here are variations on the main analysis that consider a four-signal analysis of the OZ, GHG, AA and NAT fingerprints (black), the four-signal analysis with confidence intervals derived from a CanESM2 piControl run (Methods; red) and a limited domain of analysis (100–850 hPa, 30–90° S) (blue). The vertical bars represent the 95% uncertainty (2.5th–97.5th percentiles) and the horizontal bars represent the 90% uncertainty (5th–90th percentiles).

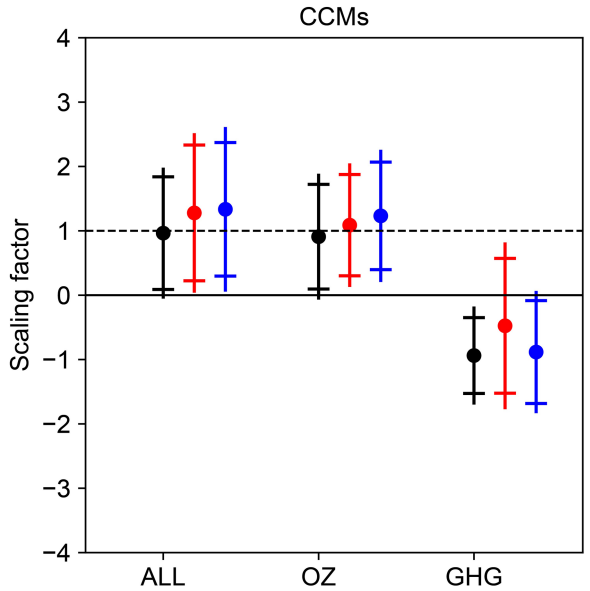

Extended Data Fig. 8 | Scaling factors from detection and attribution sensitivity tests for the CCMs. Each case shows a one-signal analysis against the ALL fingerprint, and a two-signal analysis against the OZ and GHG fingerprints. The main analysis (Fig. 4b) performs the analysis across 50 model simulations, with confidence intervals derived from a WACCM piControl run, and over the domain shown in Figs. 2, 3 (10–850 hPa, 0–90° S). The sensitivity tests shown here are variations on the main analysis that consider a subset of models that performed the fODS and fGHG sensitivity simulations (total 30 members) (black); confidence intervals derived from a WACCM piControl run containing the 11-yr solar cycle (Methods; red) and a limited domain of analysis (100–850 hPa, 30–90° S) (blue). The vertical bars represent the 95% uncertainty (2.5th–97.5th percentiles) and the horizontal bars represent the 90% uncertainty (5th–90th percentiles).

Extended Data Table 1 | Trends in ozone and circulation metrics and change-point testing

	1997	1998	1999	2000	2001	2002	2003
				TCO			
Depletion	-37.8±12.7	-35.5±12.1	-33.1±11.7	-30.7±11.4	-28.7±11.3	-26.6±11.0	-25.4±10.7
Recovery[a]	11.0±10.5	12.7±11.3	14.1±12.4	15.4±13.8	16.9±15.6	18.2±17.3	20.9±19.2
				Jet latitude			
Depletion	-0.90±0.89	-0.87±0.83	-0.83±0.78	-0.76±0.74	-0.71±0.71	-0.64±0.68	-0.57±0.65
Recovery	0.07±0.74	0.12±0.78	0.16±0.83	0.16±0.90	0.18±0.97	0.14±1.06	0.10±1.17
				SAM (reanalysis)			
Depletion	1.36±1.30	1.30±1.22	1.20±1.16	1.06±1.11	0.99±1.07	0.90±1.03	0.82±0.99
Recovery	-0.13±1.08	-0.19±1.15	-0.21±1.24	-0.15±1.35	-0.16±1.47	-0.12±1.61	-0.07±1.76
				SAM (observations)			
Depletion[b]	0.86±0.89 *(±0.75)*	0.82±0.84 *(±0.70)*	0.77±0.80 *(±0.67)*	0.68±0.76 *(±0.64)*	0.63±0.73 *(±0.61)*	0.57±0.70 *(±0.59)*	0.52±0.67 *(±0.56)*
Recovery[b]	0.04±0.74 *(±0.62)*	0.01±0.79 *(±0.66)*	0.01±0.85 *(±0.71)*	0.06±0.92 *(±0.77)*	0.06±1.00 *(±0.84)*	0.12±1.09 *(±0.91)*	0.16±1.19 *(±1.00)*
				Hadley cell edge			
Depletion	-0.57±0.45	-0.57±0.41	-0.56±0.38	-0.54±0.36	-0.51±0.34	-0.49±0.33	-0.47±0.31
Recovery	-0.03±0.37	0.01±0.39	0.04±0.41	0.07±0.44	0.09±0.47	0.11±0.51	0.13±0.56
				Jet strength			
Depletion	0.33±0.68	0.35±0.64	0.34±0.60	0.31±0.57	0.28±0.54	0.27±0.51	0.25±0.49
Recovery	0.29±0.57	0.27±0.60	0.27±0.64	0.30±0.68	0.35±0.74	0.37±0.79	0.42±0.86

Values for piecewise continuous linear trends, labelled by the change-point year, in the SON season for Antarctic TCO and in DJF for the near-surface circulation metrics. Units are: Antarctic TCO (DU per decade), jet position (degrees latitude per decade), SAM index (per decade), Hadley cell edge (degrees latitude per decade) and jet strength (m s^{-1} per decade). The uncertainty reflects the 95% confidence interval calculated as 1.96σ, where σ is the standard error of the slope.

[a]Recovery period trends with change-point years at 1996 (9.5 ± 9.9 DU per decade) and before are statistically insignificant at the 95% confidence level. 1997 is the first change-point year in which the recovery period trend becomes significant.

[b]Bracketed, italicized values represent trends with 90% confidence intervals.

Extended Data Table 2 | List of CCMs

Model	ALL	fGHG	fODS
CCMVal-2			
CAM3.5	1		
CCSRNIES	1	1	1
CMAM	3	3	3
CNRM-ACM	1		
LMDZrepro	1	1	1
MRI	2	1	1
Niwa-SOCOL	1		
SOCOL	3	1	1
ULAQ	3		
UMSLIMCAT	1	1	1
UMUKCA-METO	1		
WACCM	3	1	1
CCMI			
ACCESS CCM	2	2	2
CCSRNIES MIROC3.2	2	1	1
CESM1 CAM4Chem	3		
CESM1 WACCM	3	3	3
CHASER (MIROC-ESM)	1	1	1
CMAM	1	1	1
CNRM-CM5-3	2		
EMAC-L47MA	2		
EMAC-L90MA	1		
HadGEM3-ES	1		
IPSL-LMDZ-REPROBUS	1	1	1
MRI-ESM1r1	1		
NIWA-UKCA	5	3	2
SOCOL3	1		
UMSLIMCAT	1	1	1
UMUKCA-UCAM	2		
Total	50	22	21

The number of realizations used for each experiment from the CCMVal-2 and CCMI projects are shown. The experiments here labelled ALL, fGHG and fODS are, respectively: the REF-B2, SEN-B2c and SEN-B2b experiments in CCMVal-2; and REF-C2, SEN-C2-fGHG and SEN-C2-fODS in CCMI.